

Visualization Ability of Phase-Contrast Synchrotron-Based X-Ray Imaging Using an X-Ray Interferometer in Soft Tissue Tumors

Technology in Cancer Research & Treatment
Volume 20: 1-7
© The Author(s) 2021
Article reuse guidelines:
sagepub.com/journals-permissions
DOI: 10.1177/15330338211010121
journals.sagepub.com/home/tct


Thet-Thet -Lwin, MD, PhD^{1,2} , Akio Yoneyama, PhD³,
Hiroko Maruyama, PhD^{1,2}, and Tohoru Takeda, MD, PhD^{1,2}

Abstract

Phase-contrast synchrotron-based X-ray imaging using an X-ray interferometer provides high sensitivity and high spatial resolution, and it has the ability to depict the fine morphological structures of biological soft tissues, including tumors. In this study, we quantitatively compared phase-contrast synchrotron-based X-ray computed tomography images and images of histopathological hematoxylin-eosin-stained sections of spontaneously occurring rat testicular tumors that contained different types of cells. The absolute densities measured on the phase-contrast synchrotron-based X-ray computed tomography images correlated well with the densities of the nuclear chromatin in the histological images, thereby demonstrating the ability of phase-contrast synchrotron-based X-ray imaging using an X-ray interferometer to reliably identify the characteristics of cancer cells within solid soft tissue tumors. In addition, 3-dimensional synchrotron-based phase-contrast X-ray computed tomography enables screening for different structures within tumors, such as solid, cystic, and fibrous tissues, and blood clots, from any direction and with a spatial resolution down to 26 μm . Thus, phase-contrast synchrotron-based X-ray imaging using an X-ray interferometer shows potential for being useful in preclinical cancer research by providing the ability to depict the characteristics of tumor cells and by offering 3-dimensional information capabilities.

Keywords

phase-contrast synchrotron-based X-ray imaging, X-ray interferometer, histopathological images, rats, testicular tumors

Abbreviations

CT, computed tomography; 3D, three-dimensional; HE, hematoxylin-eosin; CCD, charged-coupled device; PSCIs, phase-contrast synchrotron-based X-ray CT images

Received: February 17, 2021; Revised: March 10, 2021; Accepted: March 19, 2021.

Introduction

Ex-vivo micro-magnetic resonance imaging has been used to generate 2- and 3-dimensional high-resolution images of tumors, but even with 9.4-T magnetic resonance scanners spatial resolution is limited to around 60 μm .¹ Micro X-ray computed tomography (CT) provides excellent anatomic imaging of bones and teeth with a spatial resolution on the sub-micrometer order,² but since biological soft tissues, including tumors, are composed of light elements, they cannot be imaged well because of their significantly weaker X-ray absorption. However, the phase-contrast X-ray CT imaging technique, which is based on phase shifts of X-rays, has the potential to overcome this problem. When an X-ray passes through an

object, its amplitude decreases and its phase shifts. In the hard X-ray region, the cross section of the phase shift is around 1000 times greater than that of absorption for light elements, such as

¹ School of Allied Health Sciences, Kitasato University, Sagami-hara, Kanagawa, Japan

² Graduate School of Medical Sciences, Kitasato University, Sagami-hara, Kanagawa, Japan

³ SAGA Light Source, Tosu, Japan

Corresponding Author:

Thet-Thet-Lwin, MD, PhD, School of Allied Health Sciences, Graduate School of Medical Sciences, Kitasato University, 1-15-1 Kitasato, Minamiku, Sagami-harashi, Kanagawaken 252-0373, Japan.
Email: ttlwin@kitasato-u.ac.jp



biological soft tissues,³ and as a result phase-contrast X-ray CT imaging is capable of providing better contrast for biological soft tissue than conventional absorption based X-ray imaging does.⁴⁻⁸

Several imaging methods, including interferometry performed with an X-ray interferometer, diffraction-enhanced imaging (Analyzer-based imaging), propagation-based method with a Fresnel pattern and Talbot interferometry with a Talbot grating interferometer, are capable of detecting object-induced phase distributions.⁹⁻¹³

A high coherence synchrotron source is an ideal means of improving the high image resolution and sensitivity of phase-contrast X-ray CT imaging for biological soft tissues, and because of its simple system set-up, the Talbot interferometry method^{7,14} has begun to be used with conventional polychromatic X-ray sources. However, the synchrotron-based crystal interferometry imaging method directly detects the phase shift by the superposition of the waves, while other methods detect the first or second spatial derivation of the phase shift. Thus, crystal interferometry has greater sensitivity for observation of biological soft tissue than other methods, because spatial distribution of phase shift (phase maps) can be obtained without integral calculation, which may amplify noise.

In previous comparative studies among absorption, diffraction-enhanced method, Talbot interferometry and crystal X-ray interferometry, the sensitivity was higher, approximately 230 times in crystal X-ray interferometer, approximately 40 times in diffraction-enhanced method, and approximately 13 times in Talbot interferometry compared to conventional absorption imaging method with monochromatic X-ray at 17.8 keV.^{15,16} Therefore, crystal interferometry is the most suitable method for making observations that require high-density resolution, such as observations of tumor microstructure and amyloid plaques. Diffraction-enhanced methods and Talbot interferometry have a wide dynamic range of density and are suitable for observation of samples containing large differences in density, such as bone and soft tissue.^{15,16}

Actually, phase-contrast synchrotron-based X-ray CT imaging using an X-ray interferometer makes it possible to visualize the fine morphological structures of biological soft tissues without using contrast agents.^{4-5,17} Histopathological imaging is a well-established approach to visualizing tissue architecture and properties down to the sub-micrometer resolution level and is widely used for tumor diagnosis, and phase-contrast synchrotron-based X-ray CT imaging has been found to provide images that close resemble conventional histopathological images.^{5,18,19}

In this article, based on a study of spontaneously occurring rat testicular tumors, we report finding that phase-contrast synchrotron-based X-ray CT imaging yielded images of soft tissue tumors whose information content was quantitatively comparable to that of histopathological images. We also demonstrated easy screening of an entire tumor from any direction by a 3-dimensional (3D) phase-contrast synchrotron-based X-ray CT method without the need for a contrast agent.

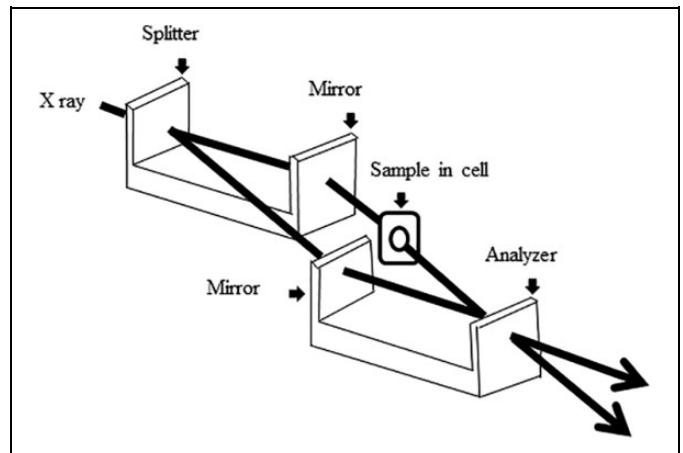


Figure 1. Phase-contrast synchrotron-based X-ray CT system with two-crystal X-ray interferometer.

Materials and Methods

Animal Preparation

Two spontaneously occurring testicular tumors obtained from aging rats (2-year-old male Wistar rats) were used as the specimens in this study. Under anesthesia, the apex of the left ventricle of the heart of each rat was surgically cannulated, and the rat's blood was replaced with physiological saline solution containing heparin in order to eliminate blood coagulation artifacts within the blood vessels. The tumor-bearing testes were quickly excised and fixed in 10% formalin for imaging.

One testis measured 14 mm in width and 20 mm in length, and the other testis measured 10 mm in width and 15 mm in length. The testes were irregular in shape and had a tense capsule, and few contusions were seen on their surface.

Phase-Contrast Synchrotron-Based X-ray CT Imaging

The phase-contrast synchrotron-based X-ray CT imaging system (Figure 1)^{20,21} consisted of an asymmetric Si (220) crystal that formed a 2-dimensional beam, a 2-crystal X-ray interferometer, a phase shifter, a target sample cell, and a lens-coupling X-ray charged-coupled device (CCD) camera with a pixel size of $18 \times 18 \mu\text{m}^2$. The field of view was set at $16 \times 13 \text{mm}^2$ to detect interference patterns.

The interferometer consisted of 2 crystal blocks containing 2 crystal wafers each. The incident X-ray beam was divided into 2 beams by the first wafer (Splitter) of the first crystal block by Laue-case X-ray diffraction, and the 2 beams were similarly reflected by the second wafer (Mirror) of the first crystal block and the first wafer (Mirror) of the second crystal block, respectively. Reflected beams were then recombined at the second wafer (Analyzer) of the second crystal block to create 2 interference beams. Placing the sample on one of the interference beam (object beam) paths produced interference fringes corresponding to the phase shift caused by the sample.

During the imaging, the specimen was placed in a sample cell filled with 10% formalin to prevent the sample from drying

shrinkage. The total image acquisition time for each sample was 2.5 hr, which included the exposure time, sample rotation time, and data transmission time. The X-ray exposure time was 9 sec per projection, and since the total number of projections was 250 over 180°, the actual X-ray exposure time was less than 40 min.

A phase map for each projection was obtained by the fringe scanning method,²² with subtraction of the background phase. The number of fringe scans was set to 3, with a 3-sec exposure time to obtain each interference pattern. The total exposure time for a phase map was 9 sec. Phase-contrast X-ray CT images were reconstructed by using a filtered back-projection algorithm with Shepp-Logan filter.^{20,21}

Experiments were carried out at the vertical wiggler beamline BL14C of the Photon Factory, High Energy Accelerator Research Organization, Tsukuba, Japan. The X-ray energy was set at 35 keV by the monochromator, and the X-ray flux in front of the sample cell was approximately 4.0×10^7 counts/sec/mm² at a ring current of 450 mA with 2.5 GeV storage energy. The density and spatial resolution of the phase-contrast synchrotron-based X-ray CT system were approximately 0.57 mg/cm³ and 26 μm, respectively.¹⁵

Histopathological Staining

After performing the phase-contrast synchrotron-based X-ray CT imaging, the specimens were sliced into 3-μm-thick sections, and the sections were stained with hematoxylin-eosin (HE) to examine their histological structure. The sections were examined with an optical microscope (Olympus FSX100; Olympus, Tokyo, Japan), and the optical microscopic images ($\times 20$) were used for comparison with the phase-contrast synchrotron-based X-ray CT image. The original color images were converted into 8-bit gray-scale images for comparison with the phase-contrast synchrotron-based X-ray CT images (PSCIs).²³

Image Analysis

The PSCIs were analyzed with real-time 3D volume-rendering software (Real INTAGE; KGT Inc., Tokyo, Japan), which contains several integrated tools for 3D image data analysis, including density measurement, data processing, and 3D display. Interactive selection of processing parameters made it easy to depict the microstructure of the tumors.

Image-manipulating software (*NIH Image* version 1.41, <https://imagej.nih.gov/nih-image>) was used to calculate mass density in regions of interest (ROI) placed on different areas of the tumors: solid areas, cystic areas, and fibrous areas.

The X-ray complex refractive index, n , is described as $n = 1 - \delta - i\beta$, where the real refractive index δ and imaginary refractive index β are related to the X-ray phase shift and X-ray absorption. δ is given by²⁴:

$$\delta = \frac{\lambda^2 r_e}{2\pi} \sum_i N_i (Z_i + f'_i),$$

where λ , r_e , N_i , Z_i , and f'_i are X-ray wavelength, classical electron radius, atomic density, atomic number, and the real part of the anomalous atomic scattering factor of element i , respectively.

By using these constituents of the refractive index, the phase shift, Δp , is given by $\Delta p = 2\pi\delta t/\lambda$, where t is the thickness of the sample. The real part of the refractive index δ was then calculated directly from the phase-shift data by using the following formula^{24,25}:

$$\delta = D\rho\lambda/2\pi t$$

Since the electron density of the sample (ρ) is almost proportional to δ ,²⁴ approximate mass density (ρ) was calculated by using the formula^{24,25}:

$$\rho = 4\pi\delta/\lambda^2 r_e N_A,$$

where δ is the real part of the refractive index, λ is X-ray wavelength, r_e is the classical electron radius, and N_A is Avogadro's number.

The area of each testicular tumor that yielded the best morphological match between the PSCIs and HE images was selected for the analysis and divided into 3 regions according to the gray-scale gradation. The mean relative gray value of each region was calculated to compare the absolute densities of the corresponding regions on the PSCIs. The gray level distribution was also measured in detail in the 3 different magnified regions.

Results

The PSCIs of the tumors showed heterogeneous dense lobulations and multiple low-density cysts in each tumor, and a few compressed seminiferous tubules were seen at the periphery of the testis as a result of almost total replacement of the testis by the tumor (Figure 2A). The lobulations appeared to be separated by high-density capsule-like structures, and they contained slightly low-density heterogeneous structures. The HE images revealed that most of the testis was occupied by the tumor, and a few compressed atrophic tubules were seen at the periphery of the testis. The tumor was composed of multiple solid nodules and cysts with dense fibrotic septa (Figure 2B and C). Thus, the HE images yielded findings very similar to the findings revealed by the PSCIs. In addition, blood clots in the vessels were visualized as multiple white spots on the PSCIs, and the HE images showed artifacts due to the cutting procedure, but the PSCIs did not.

Good linear correlations were observed between the absolute densities and the relative gray values in different areas of the tumor: solid areas, cystic areas, and fibrous areas ($r = 0.87$) in Figure 3.

We also measured absolute densities in the PSCIs (Figure 4A) and mean relative gray values in the HE images (Figure 4B) in 3 different regions of the solid soft tissue tumor (Table 1). The absolute density values for region 1, region 2, and region 3 were 1.040 ± 0.001 g/cm³, 1.078 ± 0.003 g/cm³, and 1.065 ± 0.002 g/cm³, respectively, and the corresponding mean relative gray values were 74.9 ± 15.4 , 87.6 ± 18.4 , and

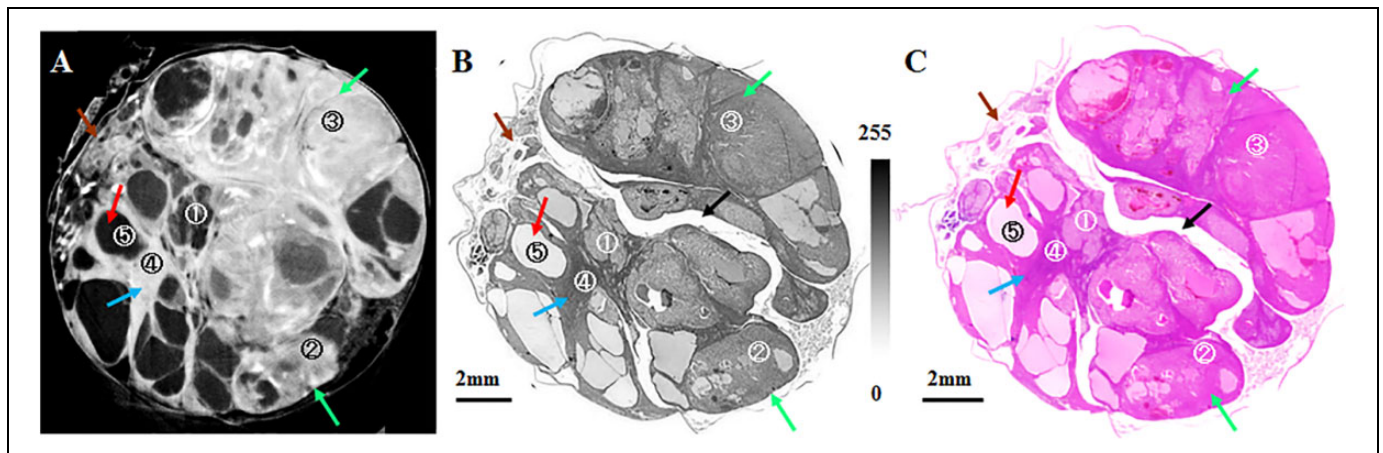


Figure 2. Tumor-bearing rat testis: (A) Phase-contrast synchrotron-based X-ray CT image; (B) corresponding histopathological (HE-stained) gray-scale image; (C) color image; periphery of the testis (brown arrow); cystic areas (red arrow); solid areas (green arrow); fibrous septa (blue arrow); artificially torn region in the HE image (black arrow).

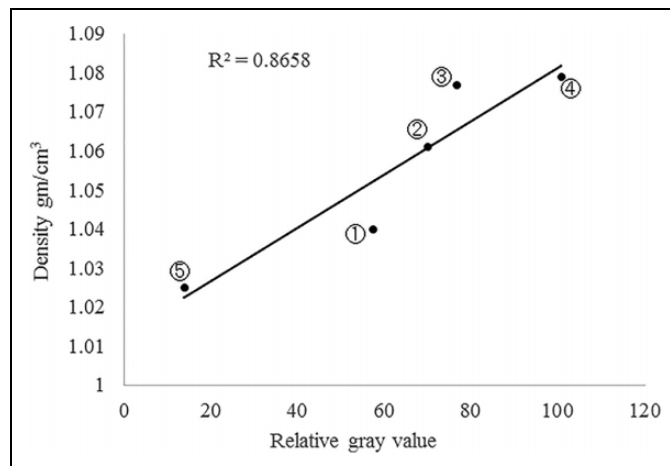


Figure 3. Correlation between the absolute densities and relative gray values of different areas of the tumor, i.e. solid portions, cystic areas, and fibrous septa, shown in Figure 2. ①: solid tumor area 1, ②: solid tumor area 2, ③: solid tumor area 3, ④: fibrous septa, ⑤: cyst.

76.9 ± 11.7 , respectively. The pixel numbers corresponding to the gray value distribution in different regions on the HE images are shown in Figure 4C.

The magnified HE images showed different types of cells within the solid soft tissue tumors, including cells containing large cytoplasmic vacuoles and small hyperchromatic nuclei (region 1), dense lymphocytes containing hyperchromatic nuclei and scant cytoplasm (region 2), and cells containing moderately enhancing abundant cytoplasm and relatively large hypochromatic nuclei (region 3) (Figure 4D). The density of the nuclear chromatin in the HE images appeared to be closely correlated with the absolute density in the PSCIs.

The excellent contrast and high resolution of the PSCIs enabled clear separation of the tumor and surrounding seminiferous tubules from any direction (Figure 5A and B). The morphology of the seminiferous tubules, blood vessels, and tunica albuginea could also be identified. The enlarged images showed

the significant tumor heterogeneity information caused by solid, cystic, blood clots and fibrous septa (Figure 5C).

Discussion

Without requiring the use of any contrast agents, phase-contrast synchrotron-based X-ray imaging provides morphological information down to a spatial resolution of approximately $26 \mu\text{m}$, which is comparable to the spatial resolution obtained by low power microscopic image. The PSCIs proved capable of depicting the various morphological structures in the soft tissue tumors, including their solid, cystic, and fibrous areas, and their hemorrhagic areas as well. In particular, minutely differing densities within the solid tumors on the PSCIs corresponded well to the different types of cells in the soft tissue tumors observed on the HE images. Quantitative comparisons between the absolute densities in the PSCIs and the relative contrast values in the HE images yielded excellent correlations, and the high-density sites on the PSCIs corresponded to the high nuclear chromatin locations on the HE images. A detailed quantitative analysis focused on the solid tumor components revealed that the density differences in the PSCIs were mainly generated by differences in the density of the nuclear chromatin on the HE images. The nuclear-cytoplasmic ratio appears to be more important to making a diagnosis of cancer than the density of the cytoplasm in tumor cells. Because cancer cells are characterized by large nuclei and a high nuclear-cytoplasmic ratio, and the latter is well-known to be a strong predictor of malignancy.²⁶ The spatial resolution provided by the high power microscopic images of $3\text{-}\mu\text{m}$ -thick HE-stained tissue sections can yield detailed cellular morphology information at less than a $1\text{-}\mu\text{m}$ resolution, which enables observation of tumor cell nuclei measuring 2- to $3\text{-}\mu\text{m}$ in diameter. Although $26\text{-}\mu\text{m}$ resolution provided by the PSCIs was considerably lower than the resolution of the histological images, the PSCIs clearly depicted the morphological structures of testis (10-14 mm in width, 15-20 mm in length) with tumor and

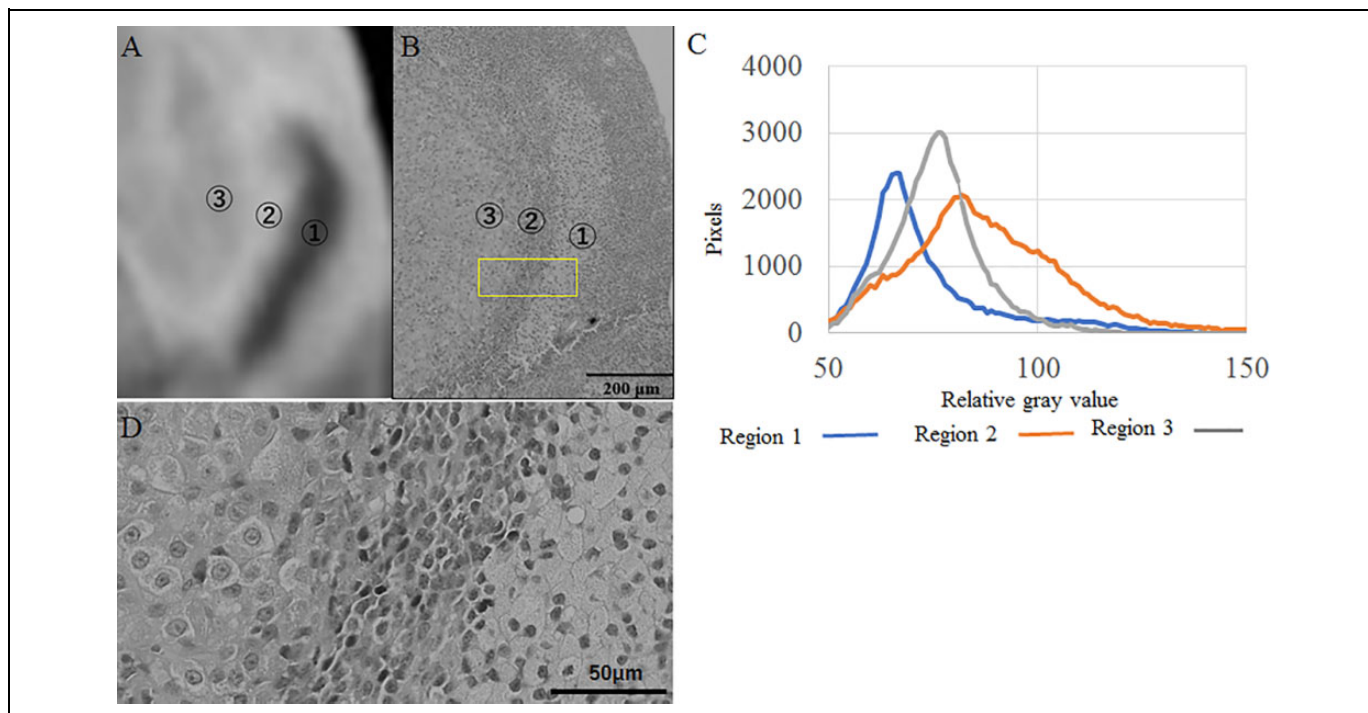


Figure 4. Magnified image of the area of the testicular tumor that yielded the closest morphological match between the phase-contrast synchrotron-based X-ray CT images and HE-stained images. (A) Phase-contrast synchrotron-based X-ray CT image, (B) gray-scale HE image, (C) gray value distribution curve of the boxed region in (B), and (D) magnified image of the boxed region in (B).

Table 1. Absolute Densities Obtained From the Phase-Contrast Synchrotron-Based X-Ray CT Image Shown in Figure 4(A) and the Relative Gray Values Obtained From the Gray-Scale HE-Stained Histopathological Images Shown in Figure 4(B).

	Region 1	Region 2	Region 3
Density (g/cm ³)	1.040 ± 0.001	1.078 ± 0.003	1.065 ± 0.002
Relative gray value	74.9 ± 15.4	87.6 ± 18.4	76.9 ± 11.7

density information that roughly corresponded to the density of the nuclear chromatin of the tumor cells.

Thus, phase-contrast synchrotron-based X-ray imaging appears to depict the characteristics of different type of cells within a solid soft tissue tumor.

Moreover, the 3D information capabilities of phase-contrast synchrotron-based X-ray imaging enable imaging of entire organs, and, in addition to revealing tumor morphology, they make it possible to detect precise density differences within tumors themselves in the form of heterogeneity that is probably attributable to differences in cell types. While histopathological staining methods are generally used in biomedical research and routine clinical practice, histological analysis of specific areas requires serial sectioning and staining, which can be labor-intensive and time-consuming and sometimes lead to inaccurate results. Phase-contrast synchrotron-based X-ray imaging can be performed repeatedly and can be used to access multiple tumor areas. Since

phase-contrast synchrotron-based X-ray imaging does not require the use of contrast agents or staining, tissue morphology is well preserved when the tissue is subsequently processed histopathologically. Thus, the 3D visualization can provide advance information that is useful in deciding on histopathological staining methods to precisely identify places to section in order to view specific areas of interest.

There are some limitations in our study. First, our dedicated imaging system can only be used with highly brilliant X-ray sources like synchrotrons and it cannot yet be used with the clinically more readily available X-ray sources such as conventional X-ray tubes. However, synchrotron-based imaging can be used as a reference standard for pathologic tissue, especially for spatial resolution on a micrometer order.²⁷ Second, the absorption by the wafers of the interferometer is not negligible when the monochromatic synchrotron 35 keV X-ray source is used. Since each wafer is 1 mm thick and has a transmission ratio of about 85%, the intensity of the outgoing interfering X-ray is reduced to about 60% by passing through 3 wafers. Thus, even with synchrotron radiation, an exposure time of several seconds is required. Moreover, current X-ray CCD cameras (lens-coupling X-ray charged couple device cameras) have limited sensitivity and low transfer speed. In order to obtain images within a shorter time, as our next step we are planning to use the interferometer containing crystal wafers as thin as 0.2 mm to reduce the absorption by the wafer, and to use a high-speed/high-sensitivity X-ray CCD camera.

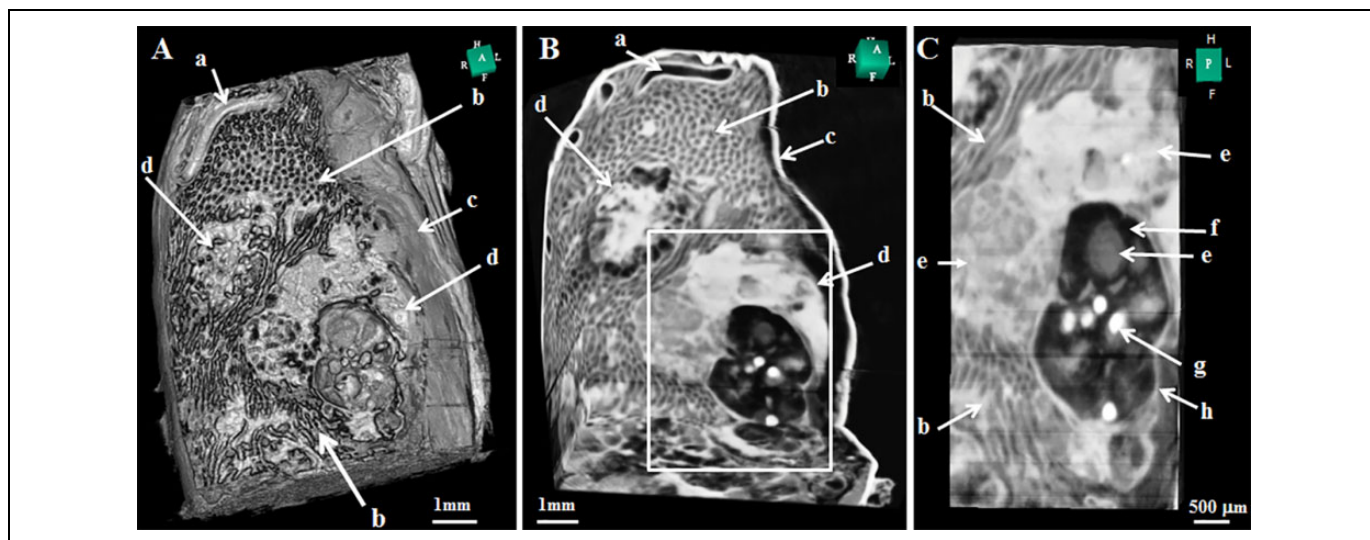


Figure 5. Three-dimensional phase-contrast synchrotron-based X-ray CT image of a tumor-bearing rat's testis. Serial cut sections of the tumor; (A) surface area, (B) internal area, (C) enlargement of the boxed region in (B); a: blood vessel, b: seminiferous tubules, c: tunica albuginea, d: tumor, e: different densities apparent of the solid area of the tumor, f: cystic area of the tumor, g: blood clot, h: fibrous septa.

Conclusions

Phase-contrast synchrotron-based X-ray imaging using an X-ray interferometer makes it possible to depict the characteristics of different type of cells in solid tissue tumor tissues, and it offers 3D information capabilities and can be used as an ancillary approach to histopathological analyses in preclinical cancer research.

Authors' Note

All animal experiments were performed in accordance with the experimental protocol approved by the President of Kitasato University through the judgment of the Animal Care and Use Committee of Kitasato University (reference number:14-02). This research was carried out with the approval (proposal nos. 2013G584, 2016G034) of the photon factory program advisory committee of the High Energy Accelerator Research Organization.

Declaration of Conflicting Interests

The author(s) declared no potential conflicts of interest with respect to the research, authorship, and/or publication of this article.

Funding

The author(s) received no financial support for the research, authorship, and/or publication of this article.

ORCID iD

Thet-Thet -Lwin, MD, PhD  <https://orcid.org/0000-0002-7225-9228>

References

- Kim E, Zhang J, Hong K, Benoit NE, Pathak AP. Vascular phenotyping of brain tumors using magnetic resonance microscopy (μ MRI). *J Cereb Blood Flow Metab.* 2011;31(7):1623-1636. doi:10.1038/jcbfm.2011.17
- Jud C, Schaff F, Zanette I, Wolf J, Fehringer A, Pfeiffer F. Dental tubules revealed with x-ray tensor tomography. *Dent Mater.* 2016;32(9):1189-1195. doi:10.1016/j.dental.2016.06.021
- Momose A, Fukuda J. Phase-contrast radiographs of non-stained rat cerebellar specimen. *Med. Phys.* 1995;22(4):375-379. doi:10.1118/1.597472
- Momose A, Takeda T, Itai Y, Hirano K. Phase-contrast X-ray computed tomography for observing biological soft tissues. *Nat Med.* 1996;2(4):473-475. doi:10.1038/nm0496-473
- Takeda T, Momose A, Hirano K, et al. Human carcinoma: early experiment X-ray CT with synchrotron radiation comparative specimen study with optical microscopy. *Radiology.* 2000;214(1):298-301. doi:10.1148/radiology.214.1.r00ja08298
- Stampanoni M, Groso A, Isenegger A, et al. Trends in synchrotron-based tomographic imaging: the SLS experience. *Developments in X-Ray Tomography V, Proceedings of the Society of Photo-Optical Instrumentation Engineers (Spie).* 2006;6318:U199-U212.
- Pfeiffer F, Weitkamp T, Bunk O, David C. Phase retrieval and differential phase-contrast imaging with low-brilliance X-ray sources. *Nat Phys.* 2006;2(4):2258-2261.
- Davis TJ, Gao D, Gureyev TE, Stevenson AW, Wilkins SW. Phase-contrast imaging of weakly absorbing materials using hard X-rays. *Nature.* 1995;373(6515):595-598.
- Fitzgerald R. Phase-sensitive X-ray imaging; new approaches that can detect X-ray phase shift within soft tissues show promise for clinical and biological applications. *Phys today.* 2000;53(7):23-28.
- Momose A. Recent advanced in X-ray phase imaging. *Jpn J Appl Phys.* 2005;44(9R):6355-6367.
- Endrizzi M. X-ray phase-contrast imaging. *Nucl Inst Meth Phys Res A.* 2018;878:88-98.
- Wilkins SW, Gureyev TE, Gao D, Pogany A, Stevenson AW. Phase-contrast imaging using polychromatic hard X-rays. *Nature.* 1996;384(6607):335-338.

13. Nugent KA, Gureyev TE, Cookson DF, Paganin D, Barnea Z. Quantitative phase imaging using hard X-rays. *Phys Rev Lett*. 1996;77(14):2961-2964.
14. Momose A. X-ray phase imaging reaching clinical uses. *Phys Med*. 2020;79:93-102. doi:10.1016/j.ejmp.2020.11.003
15. Yoneyama A, Wu J, Hyodo K, Takeda T. Quantitative comparison of imaging performance of x-ray interferometric imaging and diffraction enhanced imaging. *Med Phys*. 2008;35(10):4724-4734. doi:10.1118/1.2977543
16. Yoneyama A, Baba R, Hyodo K, Takeda T. Quantitative comparison of performance of absorption, Talbot interferometric, and crystal x-ray interferometric imaging. Electronic Presentation Online System. In: Proceedings of the ECR 2015 Conference of the European Society of Radiology; 2015:4-8. doi:10.1594/ecr2015/C-0531
17. Noda-Saita K, Yoneyama A, Shitaka Y, et al. Quantitative analysis of amyloid plaques in a mouse model of Alzheimer's disease by phase-contrast X-ray computed tomography. *Neuroscience*. 2006;138(4):1205-1213. doi:10.1016/j.neuroscience.2005.12.036
18. Huang S, Kou B, Chi Y, et al. In-line phase-contrast and grating-based phase-contrast synchrotron imaging study of brain micrometastasis of breast cancer. *Sci Rep*. 2015;5:9418. doi:10.1038/srep09418
19. Baran P, Mayo S, McCormack M, et al. High-resolution X-ray phase-contrast 3-D imaging of breast tissue specimens as a possible adjunct to histopathology. *IEEE Trans Med Imag*. 2018;37(12):2642-2650.
20. Yoneyama A, Takeda T, Tsuchiya Y, et al. A phase-contrast x-ray imaging system-with a 60 x 30 mm field of view based on a skew-symmetric two-crystal x-ray interferometer. *Nucl Instrum Methods Phys Res*. 2004;A523(1-2):217-222. doi:10.1016/j.nima.2003.12.008
21. Yoneyama A, Takeda T, Tsuchiya Y, et al. High-energy phase-contrast X-ray imaging using a two-crystal X-ray interferometer. *J Synch Rad*. 2005;12(Pt 4):534-536. doi:10.1107/S0909049505008356
22. Momose A. Demonstration of phase-contrast X-ray computed tomography using an X-ray interferometer. *Nucl Instrum Methods Phys Res*. 1995;A352:622-628. doi:10.1016/0168-9002(95)90017-9
23. Lwin T-T, Yoneyama A, Imai M, Maruyama H, Hyodo K, Takeda T. Testicular seminoma in the aged rat visualized by phase-contrast X-ray computed tomography. *Acta Radiologica Open*. 2018;7(10):2058460118806657. doi:10.1177/2058460118806657
24. Yoneyama A, Yamada S, Takeda T. Fine biomedical imaging using X-ray phase-sensitive technique. In: Gargiulo DG, Mcewan A, eds. *Advanced Biomedical Engineering*. InTech; 2011;2:107-128. doi:10.5772/20456
25. Shirai R, Kunii T, Yoneyama A, et al. Enhanced renal image contrast by ethanol fixation in phase-contrast X-ray computed tomography. *J Synch Rad*. 2014;21(4):795-800. doi:10.1107/S1600577514010558
26. Baba AI, Căto C. Tumor cell morphology. In *Comparative Oncology*. The Publishing House of the Romanian Academy [Internet]; 2007. ISBN-10:973-27-1457-3 ISBN-13:978-073-27-1457-7.
27. Wu J, Takeda T, Lwin TT, et al. Imaging renal structures by X-ray phase-contrast microtomography. *Kid Int*. 2009;75(9):945-948. doi:10.1038/ki.2009.42